Biosensors and Bioelectronics 188 (2021) 113336

Contents lists available at ScienceDirect

Biosensors and Bioelectronics

journal homepage: www.elsevier.com/locate/bios

Label-free terahertz microfluidic biosensor for sensitive DNA detection using graphene-metasurface hybrid structures

Ruiyun Zhou [a,1], Chen Wang [b,1], Yuxin Huang [a], Kang Huang [c], Yingli Wang [a], Wendao Xu [a], Lijuan Xie [a,*], Yibin Ying [a]

[a] College of Biosystems Engineering and Food Science, Zhejiang University, 866 Yuhangtang Rd., 310058, Hangzhou, Zhejiang Province, PR China
[b] Institute of Quality Standard and Monitoring Technology for Agro-products of Guangdong Academy of Agricultural Sciences, 20 Jinying Rd., 510640, Guangzhou, Guangdong Province, PR China
[c] School of Chemical Sciences, The University of Auckland, Auckland, 1142, New Zealand

ARTICLE INFO

Keywords:
Terahertz spectroscopy
Graphene
Metasurface
Microfluidics
Biosensor
DNA detection

ABSTRACT

Metasurface assisted terahertz (THz) real-time and label-free biosensors have attracted intense attention. However, it is still challenging for specific detection of highly absorptive liquid samples with high sensitivity in the THz range. Here, we incorporated graphene with THz metasurface into a microfluidic cell for sensitive biosensing. The proposed THz graphene-metasurface microfluidic platform can effectively reduce the volume of the sample solution and boost the interaction between biomolecules and THz waves, thus enhancing the sensitivity. As a proof of concept, comparative experiments using other three kinds of microfluidic cells (pure microfluidic cell, metasurface-based microfluidic cell and graphene-based microfluidic cell) were conducted to explore and verify the sensing mechanism, which evidences the high sensitivity of delicate sensing based on the hybrid graphene-metasurface THz microfluidic device. Furthermore, to perform biosensing applications on that basis, specific aptamers were modified on the graphene-metasurface, enabling DNA sequences of foodborne pathogen *Escherichia coli* O157:H7 to be recognized. Based on the THz microfluidic biosensor, 100 nM DNA short sequences can be successfully detected. The sensing results of antibiotics and DNA based on the graphene-metasurface microfluidic biosensor confirm the superiority of the proposed design and considerable promise in THz biosensing. The novel sensing platform provides the merits of enabling highly sensitive, label-free, low-cost, easy to use, reusable, and real-time biosensing, which opens an exciting prospect for nanomaterial-metasurface hybrid structure assisted THz label-free biosensing in liquid environment.

1. Introduction

Terahertz (THz) technology has inspired plentiful applications in chemical (Lin and Jarrahi, 2020; Seo and Park, 2019), medical (Ahmadivand et al., 2020), and biological sciences (Zhou et al., 2019). THz radiation with a wavelength of 0.03–3 mm and frequency range of 0.1–10 THz, is located in the electromagnetic spectrum between the microwave and infrared regions (Hafez et al., 2018). As the intramolecular and intermolecular vibrational modes of many chemicals and biological macromolecules, including pesticides, antibiotics, DNA and proteins, can be observed in the THz range, the number of THz sensing research on molecular recognition is growing (Niessen et al., 2019; Peng et al., 2018; Yang et al., 2016).

THz spectroscopy provides a lot of unique advantages, including non-destruction, non-ionization, and molecular fingerprints for sensing applications (Seo and Park, 2019; Wang et al., 2019). However, the detection sensitivity is limited for free-space THz radiation to recognize a trace amount of analytes due to mismatch between the wavelength of THz waves and size of target molecules. Hence, THz metamaterials are developed to boost the interaction of matter and THz waves by the local electric field enhancement, thus improving the sensitivity (Ahmadivand et al., 2020). As the two-dimensional equivalent of bulk metamaterials, metasurfaces have the ability to modulate magnitude, phase and polarization of electromagnetic waves at subwavelength scale (Ding et al., 2018; Huidobro et al., 2016). With the fast development of micro-nano processing technology, studies on metasurfaces have been conducted in

* Corresponding author.
E-mail address: ljxie@zju.edu.cn (L. Xie).
[1] Contributed equally to this work.

https://doi.org/10.1016/j.bios.2021.113336
Received 11 March 2021; Received in revised form 26 April 2021; Accepted 10 May 2021
Available online 14 May 2021

diverse aspects, such as wireless communication (Dai et al., 2020) and wave polarization (Li et al., 2020). Besides those inspiring advances, metasurfaces have also shown significant ability to detect minute amount of biomolecules including RNA (Narasimhan et al., 2019), DNA (Yang et al., 2018), protein (Cheng et al., 2020), and virus (Ahmadivand et al., 2018). Early researches have shown that the strong absorption of water in the THz region limits the detection performance, i.e. sensitivity and selectivity, and the process of drying samples is needed (Ahmadivand et al., 2020; Yang et al., 2016). However, most biological components exist in the water environment, so it is in urgent need to realize biosensing of liquid-based samples. Recently, microfluidic techniques have been applied to metamaterial-based THz sensing to overcome this difficulty (Alfihed et al., 2020; Hu et al., 2016). Compared with routine macroscale systems, microfluidic systems can reduce the water-induced background absorption, enabling THz waves to capture more information from the targeted substances. Moreover, microfluidic devices are low-cost, easy to operate, and capable of rapid analysis work (Hu et al., 2016).

To further improve the detection capabilities of THz devices, scientists have integrated photoelectrically tunable nanomaterials, such as graphene (Lee et al., 2020) and vanadium dioxide (Zhao et al., 2018), with metasurfaces to improve the ability of capturing target molecules. Graphene, as a kind of two-dimensional nanomaterial, has the advantages of large specific surface area, tunable optoelectronic property, and good biocompatibility, which has been employed in biosensing (Rodrigo et al., 2015). Especially, graphene exhibits a Drude-like response in the THz range, of which the photoconductivity can be changed with controlled free carrier densities. It is suitable to realize dynamic tunability (Huidobro et al., 2016; Wei et al., 2013). Hybrid materials by incorporating graphene with THz absorber with improved and tunable physicochemical properties have been reported (Xu et al., 2019). Hence, these merits make graphene of high potential in the applications of chemical sensing, modulation, and biosensing (Farid et al., 2015; Lee et al., 2020; Zeng et al., 2015). Therefore, it has great potential to achieve effective biosensing based on the hybrid structure of graphene and metasurfaces within microfluidic devices. The THz microfluidic cell (TMFC) with graphene-metasurface hybrid structure may lead to convenient, fast, real-time, quantitative, and sensitive detection without the need of drop-and-dry process. Meanwhile, the incorporation of graphene can add novel functionality to boost the performance such as via surface modification to realize specific recognition.

Over the years, biomolecular sensing, especially for the recognition

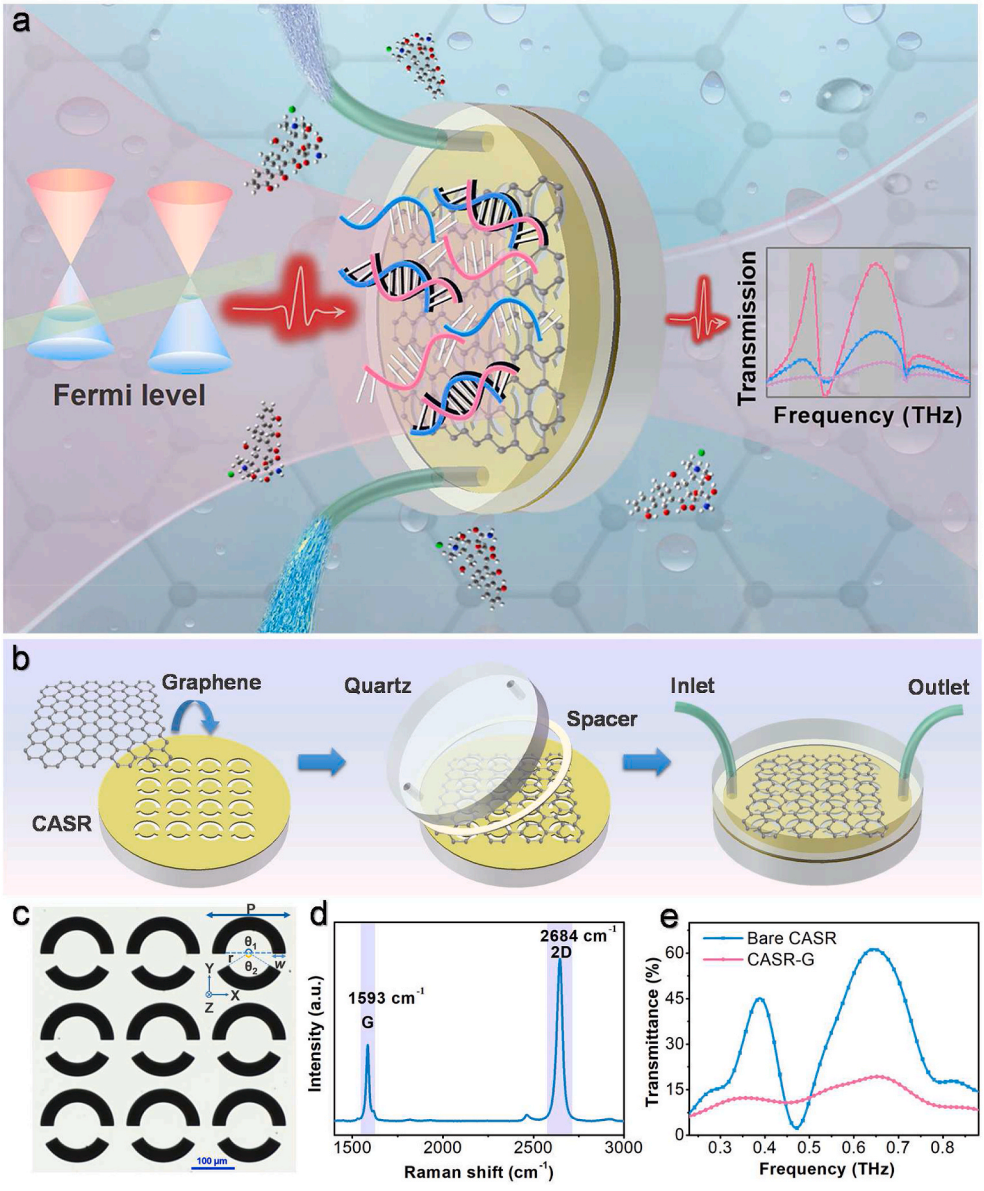

Fig. 1. CASR-graphene based THz microfluidics platform. (a) Schematic drawing showing the working principle and design of DNA biosensing based on the proposed CASR-graphene TMFC; (b) Schematic diagram of the manufacturing flow for the CASR-graphene TMFC; (c) A microscope image of the fabricated CASR metasurface. For the unit cell of the CASR arrays, outer radius R is 85 μm, inner radius r = 55 μm, width w = 30 μm, and central angles θ_1 = 180°, θ_2 = 120°, respectively. The period of the CASR arrays is P = 200 μm; (d) Raman spectroscopy of the monolayer graphene; (e) Experimentally measured transmission spectra of the CASR metasurface with/without monolayer graphene.

of DNA, has been intensively studied using various technologies, because it is a core research topic in the domain of modern genetics (Boolchandani et al., 2019). So far, interdisciplinary methods have been employed for direct and indirect DNA detection, avoiding segmental amplification or labeling (Shendure and Ji, 2008). Electrochemical method such as graphene-based field-effect transistors, and optical technologies including infrared spectroscopy, Raman spectroscopy, and surface plasmon resonance have been utilized to identify DNA molecules (Lawal, 2018; Wang et al., 2020b). However, these methods still have obvious shortcomings, such as complex fabrication process of electrodes, contact measurements, or additional marker-needed (Liu et al., 2020). As an alternative method for DNA detection, THz spectroscopy has received a lot of attention on the strength of the advances from optoelectronics, metamaterials, and novel nanomaterials (Lee et al., 2020; Wang et al., 2020a).

In this paper, we proposed a novel microfluidic platform integrating graphene with metasurface towards the goal of realizing simple, label-free, real-time, and specific biosensing in the THz region (as illustrated in Fig. 1a). By flowing appropriate volume of liquid through sensitive regions of metasurface-graphene, the interaction between THz waves and analytes can be greatly enhanced. For the proof of concept, we designed and fabricated metallic hole arrays-complementary asymmetry split ring (CASR) metasurface with graphene integrated into the microfluidic cell for sensing applications. Based on the CASR-graphene TMFC, improved sensing performance was obtained in comparison to other TMFCs, demonstrating the potential for THz sensitive liquid detection. Furthermore, to realize biosensing applications, probe aptamers were modified on the surface of CASR-graphene for constructing a biosensor to selectively detect DNA sequences, which was used to recognize the Eae gene sequences of *Escherichia coli* O157:H7 (*E. coli* O157:H7, one of the most common food-borne pathogens). The developed real-time and label-free biosensor based on the CASR-graphene TMFC shows excellent performance, enabling sensitive and selective biomolecular detection in aqueous environment in the THz region.

2. Experimental section

2.1. Materials and apparatus

Monolayer graphene grown by CVD method (Trivial Transfer Graphene) was bought from ACS Material (Medford, MA, USA). Doxycycline hydrochloride (DCH, >88%~94%), Phosphate-buffered saline (PBS), and DNA sequences were purchased from Sangon (Shanghai, China). The detailed base sequences of aptamer probe, Eae gene of *E. coli* O157:H7 (Target DNA), single-base mismatched DNA of the probe (SM DNA), InvA gene of *Salmonella enterica* (*S. enterica*), PrfA gene of *Listeria monocytogenes* (*L. monocytogenes*), ToxR gene of *Vibrio parahemolyticus* (*V. parahemolyticus*) and random DNA of the probe are shown in Table S1. Deionized water was obtained from the Milli-Q SP reagent water system (18 MΩ cm^{-1}, Millipore, Billerica, MA, USA).

Tapping-mode Atomic Force Microscopy (AFM) (Bruker AXS, Germany) was used for characterization of surface height. The Raman measurements were carried out by a LabRAM HR Evolution Raman microscope system (Horiba Jobin Yvon, Piscataway, USA), in which a He–Ne laser with a wavelength of 633 nm was utilized as the excitation source. In order to characterize the chemical doping level of graphene, Raman G peak of CASR-graphene with DCH solutions were measured. Different concentrations (0–20 mg mL^{-1}) of DCH solutions (1000 μL) were dropped onto the surface of CASR-graphene, respectively. After reaction for 0.5 h at ambient temperature, it was washed thrice by deionized water. Then, Raman spectrum was collected.

The THz spectra were collected in transmission mode utilizing a Z3-XL THz system (Zomega Corporation, East Greenbush, NY, USA), with a frequency range from 0.1 to 2.5 THz (Zhou et al., 2020). A large-aperture photoconductive antenna was used to generate THz waves, which were detected by a ZnTe electro-optic crystal. A Femto Fiber pro NIR laser (TOPTICA Photonics Inc., Germany) with a wavelength of 780 nm was utilized as the pump source, whose pulse width was less than 100 fs at a repetition rate of 80 MHz.

Before THz spectrum being measured, the warm-up process for at least 0.5 h was needed. To avoid the possible impact of moisture in the atmosphere, nitrogen gas was used to reduce the relative humidity of the testing cabinet (<1%). All the tests were performed at 23 °C (±1 °C). During the experiments, every spectrum was an average of four spectral scans and per sample was measured for three times. And an electro-controlling platform with an aligned laser diode was employed to make sure that each transmission spectrum was measured from a fixed location of the sample.

2.2. Preparation of the hybrid graphene-metasurface

The CASR metasurface is depicted in Fig. 1b, consisted of Au with a thickness of 100 nm, quartz substrate with a thickness of 1000 μm. The Au film was pre-deposited on the quartz substrate, and then CASR arrays were fabricated on the surface of Au film using standard photolithography methods, of which the detailed process information and the photography can be found in Figs. S1–S2. Each unit cell of the arrays consists of two split Au hole rings (outer radius R is 85 μm, inner radius r = 55 μm, width w = 30 μm) with central angles $\theta_1 = 180°$ and $\theta_2 = 120°$, respectively. The period of the CASR arrays is P = 200 μm (Fig. 1c).

In order to prepare the CASR-graphene hybrid metasurface, monolayer graphene with a size of 10 mm × 10 mm was gently released onto the surface of water and kept still for at least 2 h at room temperature. Then it was transferred onto the surface of CASR metasurface by matching the graphene area with the CASR structure. The CASR-graphene hybrid metasurface was baked in an oven at 100 °C for 20 min. Then, acetone was used to remove the polymethyl methacrylate (PMMA) layer on the top of graphene. Finally, the CASR-graphene hybrid metasurface was ready for assembling into a microfluidic cell.

2.3. Simulation of CASR-graphene

The numerical simulations were performed using FDTD Solutions 8.18.1365 (Lumerical Solutions, Inc. Vancouver, Canada). In the simulation model, the quartz substrate was set as a lossless dielectric with dielectric permittivity $\varepsilon = 3.84$ (Davies et al., 2018), and the Au film was modeled as perfect electric conductor. The polarization direction of incident THz radiation was set along y axis (as illustrated in Fig. 1c). The transmission $T(\omega)$ was defined by the following formula: $T(\omega) = |E_s(\omega)/E_r(\omega)|^2$, where $E_s(\omega)$ and $E_r(\omega)$ are the THz electric field amplitude after the fast Fourier transformation of THz pulses of the sample and reference, respectively.

The finite element method was used for analyzing the optoelectronic behavior of graphene, and the material parameters were based on the 3D graphene model in the FDTD system, of which the photoconductivity of graphene at THz frequencies can be expressed by Kubo formalism (Hanson, 2008). The Fermi level of graphene was set as from 0 meV to −100 meV, and the thickness of which was set as 1 nm. The detailed parameters of graphene can be found in Table S2.

2.4. Methods of THz microfluidic sensing

A quartz-based microfluidic cell was bought from PIKE Technologies Inc. (USA), consisted of two quartz windows with a thickness of 1000 μm, Teflon spacers with thickness of 10 μm and 25 μm, and two plastic hoses as inlet and outlet for the microchannel. One of the quartz windows was replaced by quartz with CASR-graphene structure, of which the fabrication process is introduced above. The configuration of the CASR-graphene THz microfluidic cell was schematically shown in Fig. 1b.

To effectively reflect the signal response for the measured sample,

the effective transmission area $S_{(f1\text{-}f2)}=\int_{f1}^{f2} T(f)df$ is defined in our research, which indicates the transmission strength within a certain frequency range. Here, f means the THz frequency, $T(f)$ means THz transmittance function, $f1$ and $f2$ correspond to the initial frequency and end frequency. Different types of TMFCs used in our research have notably different $S_{(f1\text{-}f2)}$ within the same frequency range due to different structure composition. To focus on the changes induced by DCH and have a meaningful comparison for the sensing performance of these TMFCs, the relative change rate of $S_{(f1\text{-}f2)}$ was defined as $\Delta S/S_0 = [S^{DCH}_{(f1-f2)}\text{-}S^{water}_{(f1-f2)}]/S^{water}_{(f1-f2)}$, where $S^{DCH}_{(f1-f2)}$ indicates the effective transmission area of DCH aqueous solutions at a certain concentration in the microfluidic cell at the frequency band from $f1$ to $f2$, and $S^{water}_{(f1-f2)}$ indicates the effective transmission area of water in the same kind microfluidic cell at the frequency band from $f1$ to $f2$. To reflect the intensity difference of the two resonant modes for CASR-graphene structure, the difference of the transmitted energy intensity of the two resonant peaks was calculated and defined as $D\text{-}value = S_{(0.44\text{-}0.54)}\text{-}S_{(0.26\text{-}0.36)}$.

In the DCH sensing tests, a series of DCH aqueous solutions with concentrations ranging from 0 to 10000 mg L^{-1} (deionized water, 0.1, 1, 10, 100, 1000, and 10000 mg L^{-1}) were prepared by dissolving appropriate amount of DCH powder in deionized water. Desired DCH aqueous solution with appropriate volume was injected into the microfluidic cell to fill the entire sensing chamber before measurement.

The procedure of preparing the DNA biosensor is illustrated in Fig. 6a and briefly described next. The aptamer probe with a 5′ pyrene modification, target DNA, SM DNA, InvA gene of *S. enterica*, PrfA gene of *L. monocytogenes*, ToxR gene of *V. parahemolyticus* and random DNA are dissolved in PBS to form the mother liquor reagents with a concentration of 100 μM, respectively. Aptamer probe solution was injected into the cell of proposed CASR-graphene TMFC, and then was left to incubate for 2 h at room temperature to ensure the effective adsorption of aptamers onto the surface of CASR-graphene, after which it was gently washed thrice by PBS to removed unbounded aptamers. After that, different concentrations (0, 0.1, 1, 5, 10, 50, and 100 μM) of DNA samples (target DNA, SM DNA, InvA gene of *S. enterica*, PrfA gene of *L. monocytogenes*, ToxR gene of *V. parahemolyticus* or random DNA) were injected into the microfluidic cell, respectively. After reaction for 0.5 h at ambient temperature, it was washed thrice again by PBS to remove un-hybridized DNA samples. Then, the corresponding spectra were measured through THz-TDS system, and the immobilization of aptamer probe and the hybridization of DNA were proved further using AFM.

3. Results and discussion

3.1. Properties of CASR-graphene

The experimental transmission spectra of the CASR is shown in Fig. 1e. It has two resonance peaks at 0.39 THz with Fano-like response and 0.65 THz with dipolar-like response, respectively. The experimental transmission with two peaks is consistent with the simulation results (Fig. 2a), and the difference in intensity results from the slight absorption of quartz substrate and the system parameter error between simulation and experiment environment. The physical mechanism of CASR has been illustrated in previous findings (Singh et al., 2011; Zentgraf et al., 2007). And the THz near-field properties of the CASR is shown in Fig. S3. Raman spectroscopy was used to confirm the properties of the single-layer graphene. As shown in Fig. 1d, an obvious high-intensity 2D peak (~2684 cm^{-1}) and a low-intensity G peak (~1589 cm^{-1}) can be observed, where the intensity ratio ($I_{2D}/I_G > 2$) and single Lorentzian shape of 2D peak confirm the single-layer graphene with high quality (Ferrari et al., 2006). After transferring graphene on the surface of CASR, the original resonance peaks are significantly attenuated, and the transmittance of the second peak at 0.65 THz is damped from 61% to 19% (see Fig. 1e). Thus, the apparent change of the transmission spectrum should be due to the introduction of the conductive monolayer graphene.

To better understand the modulation mechanism of CASR-graphene, FDTD simulations were conducted. Since the photoconductivity of graphene in the THz region can be effectively tuned by changing the Fermi

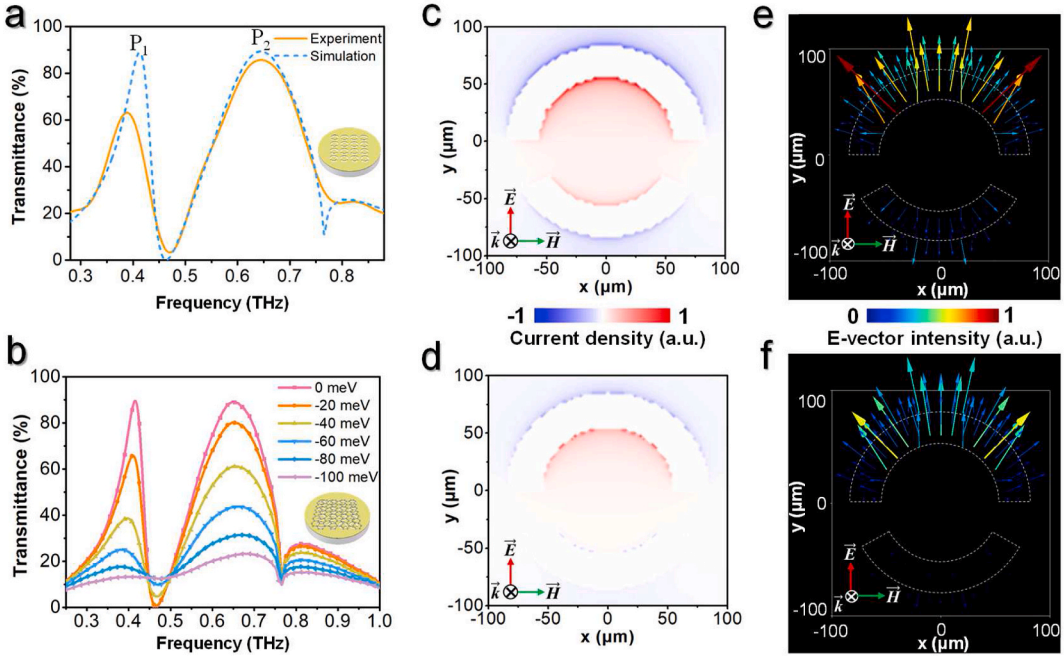

Fig. 2. Sensing principle of the CASR-graphene TMFC. (a) Experimental and simulated transmission spectra of the CASR metasurface; (b) Simulated transmission spectra for CASR-graphene with Fermi levels ranging from 0 to −100 meV; (c)–(d) Simulated current density distribution at the first peak (0.39 THz) of the CASR-graphene with the Fermi level at 0 and -40 meV, respectively; (e)–(f) Simulated electric field vector at the first peak (0.39 THz) of the CASR-graphene with the Fermi level at 0 and -40 meV, respectively.

level of graphene according to Kubo equation (Hanson, 2008). CASR-graphene with different Fermi levels were focused in the simulations. Fig. 2b illustrates the numerical results of CASR-graphene. The transmittance intensity keeps falling as the Fermi level changes from 0 to −100 meV, where the transmittance peak intensity decreases from 89% to 13% at 0.39 THz, and from 89% to 23% at 0.65 THz, respectively. By contrast, THz response of SiO_2-graphene with various Fermi levels was also simulated (Fig. S4). The attenuation effect of graphene on quartz with transmittance decreasing from 89% to 56% at 0.65 THz is weaker than that of CASR-graphene. Therefore, the graphene with higher conductivity has lower THz transmission and there is some interaction between graphene and CASR. To illustrate the interaction mechanism of CASR-graphene, we further investigated the surface current densities and electric field vector at the first peak of 0.39 THz with Fermi level of 0 and -40 meV (as shown in Fig. 2c–f, respectively). From the simulated spectra and the electric field intensity analysis, graphene with higher absolute value of Fermi level would have higher conductivity, which could greatly reduce the quantity of electric charge accumulated on both sides of the CASR, thus damping the THz transmittance and field strength. Additionally, when the Fermi level moves to its Dirac point, the damping effect is suppressed, and the resonance phenomenon becomes apparent (Zeng et al., 2015). Considering the fact that the Fermi levels of graphene can also be doped by chemical molecules (Liu et al., 2011), graphene integrated with CASR metasurface can be employed as the sensing medium for converting chemical signals of analytes to the optoelectronic signals, which is feasible for sensing applications in the THz region.

3.2. Sensing principle of CASR-graphene TMFC

To evaluate the sensing performance of the proposed CASR-graphene TMFC (as shown in Fig. 3a), DCH, one type of the broad-spectrum tetracycline antibiotics, was chosen as an example. DCH aqueous solutions with concentrations of 0, 0.1, 1, 10, 100, 1000, and 10000 mg L^{-1} were tested. For comparison, the DCH aqueous solutions were also detected based on the pure TMFC, CASR-based TMFC, and graphene-based TMFC, respectively. The composition of these three kinds of TMFCs is illustrated in Figs. S5a–c. The measured transmission spectra using these four TMFCs are shown in Fig. 3b and Figs. S5d–f, respectively. The overall trend of the results is that the transmittance increases with increasing DCH concentration. Compared with the pure TMFC, CASR-based TMFC, and graphene-based TMFC, the sensing results based on CASR-graphene TMFC have more remarkable change of transmittance, which is clearly distinguished between different DCH concentrations. Moreover, the resonant peaks of CASR gradually appear with the increase of the concentration of DCH solutions based on the CASR-graphene based TMFC (Fig. 3b), which is different from the amplitude change or frequency shift in routine metamaterials-based detection for aqueous solution. To illustrate it better, $S_{(f1\text{-}f2)}$ and *D-value* are defined to describe the effective area change of transmittance and resonant intensity, respectively. According to the THz transmission spectra of CASR-graphene, we chose 0.25 THz as $f1$, and 0.55 THz as $f2$, using frequency band from 0.25 THz to 0.55 THz as the region of interest, where the main resonant responses of CASR-graphene are included, and the characteristic change is apparent with high signal-to-noise ratio. And $D\text{-}value = S_{(0.26\text{-}0.36)} - S_{(0.44\text{-}0.54)}$. As shown in Fig. 3c, higher values of $S_{(f1\text{-}f2)}$ and *D-value* (from 0.09 to 0.23) are obtained when the concentration of DCH solution is increased from 0.1 mg L^{-1} to 10000 mg L^{-1}, which arises from the weakened conductivity of graphene. For better comparing the sensing performance of these four TMFCs with different average transmittance, corresponding change rates of effective transmission area ($\Delta S/S_0$) with different DCH concentrations were calculated and displayed in Fig. 3d. It can be observed that $\Delta S/S_0$ increases monotonously with the increase of the concentration of DCH aqueous solutions. 0.1 mg L^{-1} DCH solutions were successfully detected in the measurements using CASR-graphene TMFC, showing a sensitivity better than previously reported results using THz microfluidics (Zhang et al., 2019). However, the sensing results based on other three TMFCs show minor changes. For pure TMFC and CASR-based TMFC, the slight increase in transmittance is mainly due to the changes in the refractive index and the absorption coefficient of different DCH solutions. By contrast, the transmission change based on graphene-based TMFC is more obvious than that based on pure TMFC and CASR-based TMFC, resulting from the photoconductivity change of graphene. Nevertheless, it is much smaller than the change based on CASR-graphene based TMFC, revealing the enhanced sensing ability of the hybrid structure of CASR-graphene.

Although the refractive index and the absorption coefficient of DCH

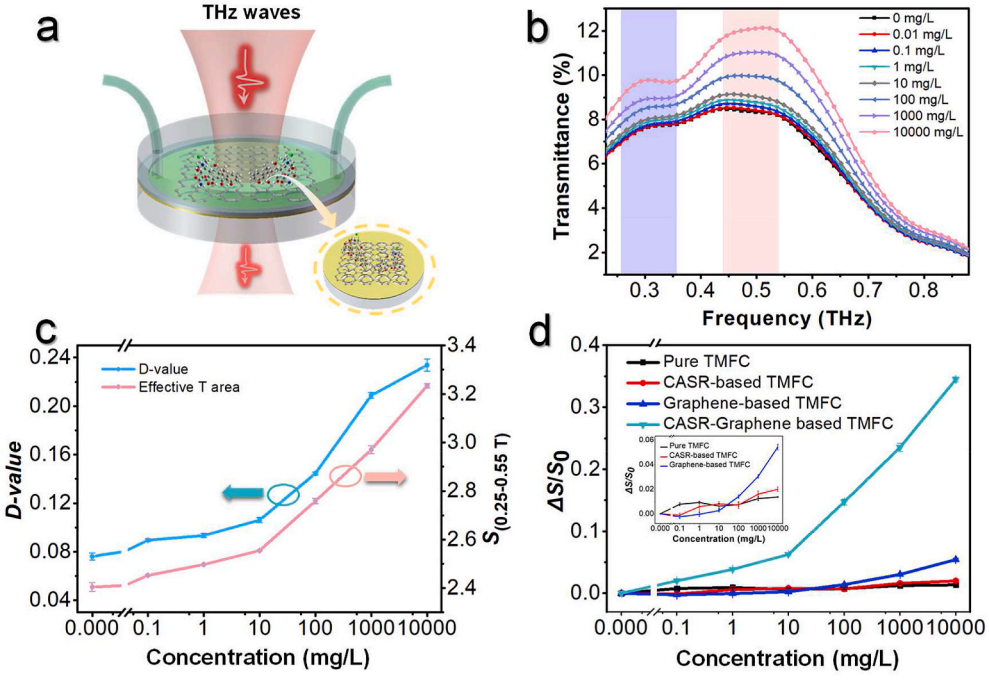

Fig. 3. Detection ability of DCH aqueous solutions using the CASR-graphene TMFC. (a) Schematic diagram of DCH sensing based on the CASR-graphene TMFC; (b) Measured THz transmission spectra of DCH aqueous solutions at different concentrations; (c) Effective transmission areas in 0.25–0.55 THz and effective resonance difference values between 0.26–0.36 THz and 0.44–0.54 THz versus different DCH concentrations; (d) Relative change rate in effective transmission areas of the four types of TMFCs for DCH aqueous solution detection versus DCH concentrations. The inset is an enlarged view of the relative change rate in effective transmission areas.

solutions decrease with the increase of their concentrations, the main factor was the chemical doping effect of DCH on CASR-graphene by comparing the sensing results of four kinds of microfluidic cell in Fig. 3d. To provide a chemical rationale for these remarkable results and verify the effectiveness of the doping effect of DCH molecules, non-covalent surface transfer doping (Bianco et al., 2020) was illustrated in Fig. 4a, and Raman spectra were employed to characterize the doped graphene samples. As shown in Fig. 4a, the Fermi level of *p*-type doped graphene could move to its Dirac point due to the *n*-type doping by absorbed molecules through non-covalent surface force, including van der Waals' force, π-π stacking and H-bonds. In this case, a larger number of molecules could shift the Fermi level nearer to Dirac point, resulting in a more pristine graphene with lower photoconductivity, thus achieving higher transmittance and more prominent resonance of the CASR-graphene TMFC, which corresponds to the results in Fig. 3b. It is well known that Raman G peak of monolayer graphene is more sensitive to doping effect (Das et al., 2008). G peak shift was chosen to demonstrate the doping effect of DCH solutions here. As shown in Fig. 4b, Raman G peak of CASR-graphene shifted from 1592.9 cm^{-1} to 1582.4 cm^{-1} with the concentration of DCH solutions from 0 to 20 mg mL^{-1}, demonstrating that more DCH molecules made the p-doped graphene more pristine. The doping effect derives from the charge transfer from DCH molecules toward graphene, and the results are consistent with previous reports (Bianco et al., 2020; Das et al., 2008; Sousa et al., 2020; Wang et al., 2020c). In addition, Fig. 4c presents THz transmission spectra taken with/without DCH molecular doping at a concentration of 1000 mg L^{-1}, and after water rinsing for reusable CASR-graphene. The transmittance spectra of CASR-graphene before DCH doping and after water rinsing are essentially coincident, demonstrating good reusability of the CASR-graphene TMFC. It's worth emphasizing that the synergistic effect of CASR and graphene can greatly enhance the detection capability of the proposed THz microfluidic cell. Additionally, the CASR-graphene and microfluidic design increases the interactions between THz waves and analytes, and effectively reduces the volume of water. Therefore, the sensing results of the proposed THz CASR-graphene microfluidic platform and the Raman spectroscopy characterization confirm that THz signal differences are mainly due to the Fermi level changes of graphene by biomolecular chemical doping, which have little to do with the refractive index and absorption coefficient of samples. The differences can be enlarged by the local electric field enhancement of CASR structure, enabling superior sensitivity in the detection of trace amount of biochemical analytes.

3.3. Biosensing by CASR-graphene TMFC

To verify the feasibility of the proposed CASR-graphene TMFC for biosensing applications, CASR-graphene was modified with probe DNA for specifically recognizing target DNA sequences of *E. coli* O157:H7. The acquired transmission spectra of CASR-graphene before and after modification are shown in Fig. S6. The pyrene group of the probe DNA can be absorbed on the surface of graphene through π-π stacking, leading to a lower conductivity of graphene, and then enabling a higher THz transmission. The immobilization of DNA probe and the hybridization of probe and the target DNA of the Eae gene sequences of *E. coli* O157:H7 are confirmed by AFM height images, as shown in Fig. 5b. AFM measurements of 3.5 μm × 3.5 μm area including with and without probe/target DNA molecules are chosen to represent the difference. The probe region shows that the structures are roughly a few hundred nanometers wide, and average of 30–50 nm tall, and the hybridization regions of 50–80 nm tall, whereas the no-probe/target DNA region does not have a distinguishable structure except for a few nanometer tall ridges (<10 nm), which might come from the uneven surface of the substrate. These tall structures are assumed to be piles of probe and DNA molecules binding to the graphene surface, of which the results are consistent with the previous literature (Farid et al., 2015; Xu et al., 2019).

The results of detecting DNA molecules with concentrations of 0.1 μM–100 μM are presented in Fig. 6a. An increase of the transmission can be clearly observed. Moreover, the change ratio of effective area monotonically increases with the increase of concentrations (Fig. 6b). These results mainly derive from the surface electron transfer between DNA molecules and graphene through non-covalent adsorption (Mattioli et al., 2021). Furthermore, to assess the specificity of the CASR-graphene TMFC biosensor, comparative tests for other kinds of DNA were conducted. Fig. 6c presents that the change ratio of effective transmittance area in response to target DNA is much higher than that for SM DNA, InvA gene of *S. enterica*, PrfA gene of *L. monocytogenes*, ToxR gene of *V. parahemolyticus* and random DNA. Through comparing the difference between the weak response from the control experiments and significant signal change from the target DNA (shown in Fig. 6d), high selectivity of the CASR-graphene TMFC biochemical sensor can be verified, revealing its great potential for active detection of DNA sequences of *E. coli* O157:H7 with high performance.

For biosensing applications, it is especially crucial to guarantee the system stability. In order to assess the stability of THz system, we further conducted the repeatable measurement of dry air at room temperature (23 ± 1 °C). The spectra shown in Fig. S7 were collected constantly for 240 min over a 5 min interval. Fig. S7 demonstrates that the electric field peak amplitudes were concentrated on the mean value of 133.1 with the RSD of 0.8%, which is caused by the internal interference of the THz-TDS instrument. By contrast, the RSD of the electric field peak amplitudes between 0 and 100 nM DNA sequences of *E. coli* O157:H7 is 3.2%, which is more significant than the system disturbance. The above biosensing results amply confirm the robust feasibility for the sensitive detection of DNA sequences of pathogenic bacteria based on the proposed CASR-graphene TMFC, which is an excellent real-time and label-free biosensing platform for DNA sensing. Compared with the previous research on integrating microfluidic channel with merely a single metamaterial, the proposed CASR-graphene TMFC can capture minor

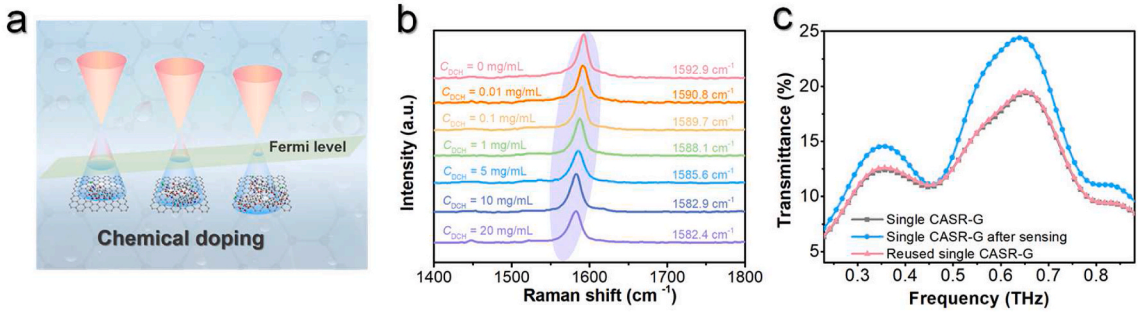

Fig. 4. Chemical doping of CASR-graphene. (a) Schematic illustration of the position of the Dirac point and the Fermi level as a function of chemical doping; (b) Raman spectra of the monolayer graphene on CASR with different DCH concentrations; (c) Measured THz transmission spectra of the CASR-graphene before measurement, after measurement, and after rinsing in water for reuse for DCH detection in the CASR-graphene TMFC.

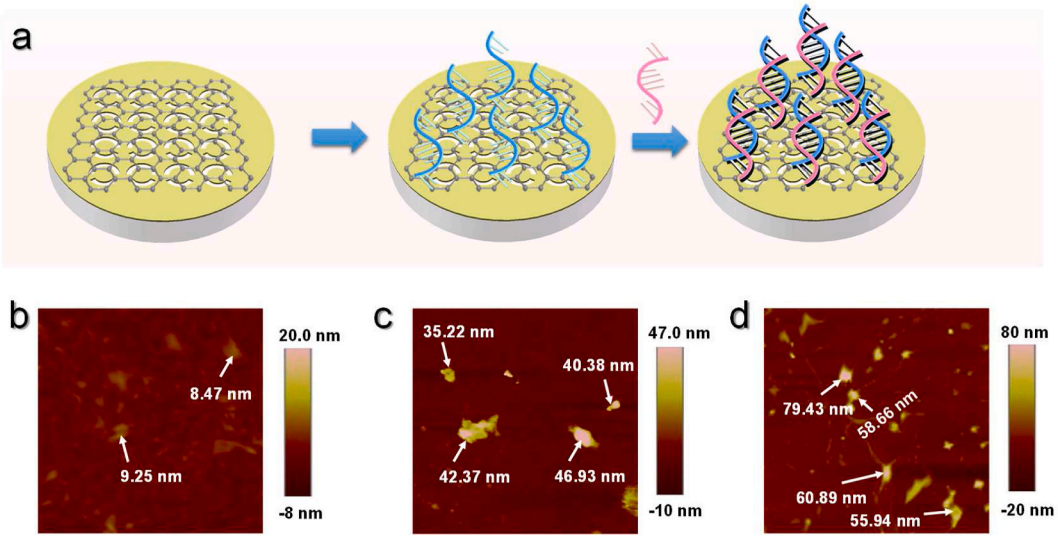

Fig. 5. The preparation process of DNA biosensing. (a) Schematic illustration of the sample preparation of immobilizing DNA probe on CASR-graphene used as an aptamer biosensor to recognize the Eae gene sequences of *Escherichia coli* O157:H7; (b) AFM height image of CASR-graphene without probe DNA; (c) AFM height image of CASR-graphene with probe DNA; (d) AFM height image of CASR-graphene with probe DNA and target DNA.

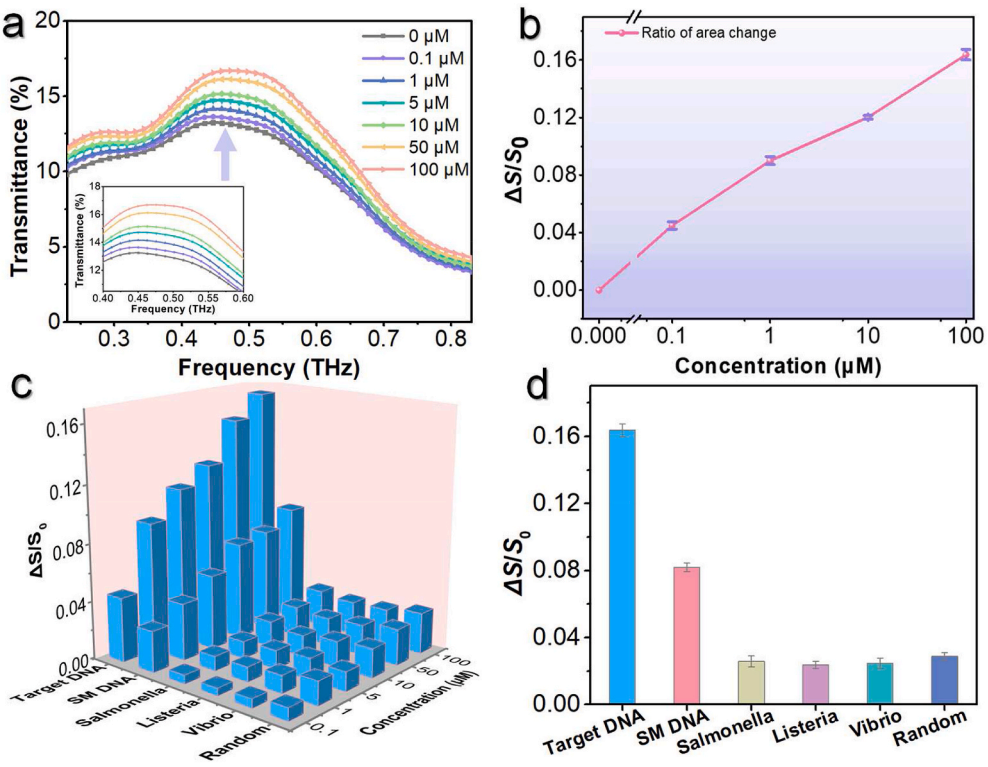

Fig. 6. Biosensing of the Eae gene sequences of *Escherichia coli* O157:H7 using CASR-graphene TMFC. (a) Measured THz transmission spectra of the target DNA at different concentrations using CASR-graphene TMFC. The inset is an enlarged view of the transmission spectra; (b) Relative changes in effective transmission areas for target DNA aqueous solution detection versus different concentrations; (c) Specificity of the CASR-graphene TMFC biosensor for detecting target DNA, single-base mismatched DNA of probe, InvA gene of *Salmonella enterica*, PrfA gene of *Listeria monocytogenes*, ToxR gene of *Vibrio parahemolyticus*, and random DNA of probe at different concentrations; (d) Specificity of the CASR-graphene TMFC biosensor for detecting these samples at the concentration of 100 μM. Error bars indicate the standard deviation (n = 3).

changes of trace biomolecules through chemical doping of graphene, thus increasing the detection sensitivity. In order to further improve the detection sensitivity for real applications, the following three aspects can be considered in the subsequent research: Firstly, excited mode with extremely confined electromagnetic field can be obtained through designing appropriate arrays and geometrical parameters; Secondly, dual-layer graphene can be used to enhance the chemical signal acquisition ability; Last but not least, deep learning method, such as the deep convolution neural network, can be combined with the optimization selection of frequency band to further extract effective THz signal and characteristic value, which could reflect the concentration variation of target molecules. For the practical application concerns of the device, such as the fabrication cost and disturbance of environmental chemical molecules, other nanomaterials or smart materials, such as carbon nanotubes and smart hydrogels, could be alternative candidates for future THz devices. Highly aligned and large carbon nanotube film can be produced using vacuum filtration method, which is simple and cost-effective (He et al., 2016). In addition, chemical doping can tune the conductivity of the carbon nanotube layers, which can transform the chemical information into optoelectronic signal (Komatsu et al., 2017). Smart hydrogels can be used to transform the target-induced stimuli into detectable signals by the bio-recognition of three-dimensional network,

which has the advantages of a large surface-area-to-volume ratio, functional versatility, and high stability to the environmental disturbance (Zhou et al., 2021). In short, the simplicity of this design can make it adopted into the standard THz-TDS system with low cost and robustness for real liquid-based detection.

4. Conclusion

In summary, a novel and multifunctional CASR-graphene based THz microfluidic cell was proposed as an effective platform for biosensing in liquid environment, which enables real-time and label-free molecular detection with high sensitivity and selectivity. Compared with previous THz sensing methods, this strategy avoids the need of drying samples, which is more convenient and direct. Through incorporating graphene with CASR metasurface into a microfluidic cell, the detection sensitivity was greatly enhanced. The results showed that trace amount of chemical molecules can be successfully discriminated. Furthermore, DNA biosensor was constructed by modifying specific aptamers on graphene-CASR, realizing the selective detection of 100 nM DNA solution. The proposed metasurface-nanomaterial design has potential for broader applications in real liquid-based biosensing in the THz region and could advance the development of THz microfluidic lab-on-a-chip. Additionally, the hybrid CASR-graphene sensing platform will offer diverse area for future studies, not only for ultrasensitive biomedical detection but also for understanding the interfacial photoelectric behavior of novel nanomaterials.

CRediT authorship contribution statement

Ruiyun Zhou: Designing, Conceptualization, Investigation, Formal analysis, Writing – original draft. **Chen Wang:** Designing, Conceptualization, Investigation, Formal analysis, Writing-revision. **Yuxin Huang:** Experimental design for THz microfluidic cell. **Kang Huang:** Supervision, Writing – original draft. **Yingli Wang:** Formal analysis. **Wendao Xu:** Formal analysis. **Lijuan Xie:** Supervision, Writing – original draft. **Yibin Ying:** Supervision, Writing – original draft.

Declaration of competing interest

The authors declare that they have no known competing financial interests or personal relationships that could have appeared to influence the work reported in this paper.

Acknowledgements

This work was supported by the National Science Found for Distinguished Young Scholars of Zhejiang Province (No. LR18C130001).

Appendix A. Supplementary data

Supplementary data to this article can be found online at https://doi.org/10.1016/j.bios.2021.113336.

References

Ahmadivand, A., Gerislioglu, B., Ahuja, R., Mishra, Y.K., 2020. Mater. Today 32, 108–130.
Ahmadivand, A., Gerislioglu, B., Tomitaka, A., Manickam, P., Kaushik, A., Bhansali, S., Nair, M., Pala, N., 2018. Biomed. Opt. Express 9 (2), 373–386.
Alfihed, S., Holzman, J.F., Foulds, I.G., 2020. Biosens. Bioelectron. 165, 112393.
Bianco, G.V., Sacchetti, A., Milella, A., Grande, M., D'Orazio, A., Capezzuto, P., Bruno, G., 2020. Carbon 170, 75–84.
Boolchandani, M., D'Souza, A.W., Dantas, G., 2019. Nat. Rev. Genet. 20 (6), 356–370.
Cheng, R., Xu, L., Yu, X., Zou, L., Shen, Y., Deng, X., 2020. Opt. Commun. 473, 125850.
Dai, J.Y., Yang, L.X., Ke, J.C., Chen, M.Z., Tang, W.K., Li, X., Chen, M., Wu, Z.H., Cheng, Q., Jin, S., Cui, T.J., 2020. Laser Photon. Rev. 14 (6), 1900133.
Das, A., Pisana, S., Chakraborty, B., Piscanec, S., Saha, S.K., Waghmare, U.V., Novoselov, K.S., Krishnamurthy, H.R., Geim, A.K., Ferrari, A.C., Sood, A.K., 2008. Nat. Nanotechnol. 3 (4), 210–215.
Davies, C.L., Patel, J.B., Xia, C.Q., Herz, L.M., Johnston, M.B., 2018. J. Infrared Millim. Te. 39 (12), 1236–1248.
Ding, F., Zhong, S., Bozhevolnyi, S.I., 2018. Adv. Opt. Mater. 6 (9), 1701204.
Farid, S., Meshik, X., Choi, M., Mukherjee, S., Lan, Y., Parikh, D., Poduri, S., Baterdene, U., Huang, C.E., Wang, Y.Y., Burke, P., Dutta, M., Stroscio, M.A., 2015. Biosens. Bioelectron. 71, 294–299.
Ferrari, A.C., Meyer, J.C., Scardaci, V., Casiraghi, C., Lazzeri, M., Mauri, F., Piscanec, S., Jiang, D., Novoselov, K.S., Roth, S., Geim, A.K., 2006. Phys. Rev. Lett. 97 (18), 187401.
Hafez, H.A., Kovalev, S., Deinert, J.C., Mics, Z., Green, B., Awari, N., Chen, M., Germanskiy, S., Lehnert, U., Teichert, J., Wang, Z., Tielrooij, K.J., Liu, Z.Y., Chen, Z. P., Narita, A., Mullen, K., Bonn, M., Gensch, M., Turchinovich, D., 2018. Nature 561 (7724), 507–511.
Hanson, G.W., 2008. J. Appl. Phys. 103 (6), 064302.
He, X., Gao, W., Xie, L., Li, B., Zhang, Q., Lei, S., Robinson, J.M., Haroz, E.H., Doorn, S.K., Wang, W., Vajtai, R., Ajayan, P.M., Adams, W.W., Hauge, R.H., Kono, J., 2016. Nat. Nanotechnol. 11 (7), 633–638.
Hu, X., Xu, G., Wen, L., Wang, H., Zhao, Y., Zhang, Y., Cumming, D.R.S., Chen, Q., 2016. Laser Photon. Rev. 10 (6), 962–969.
Huidobro, P.A., Kraft, M., Maier, S.A., Pendry, J.B., 2016. ACS Nano 10 (5), 5499–5506.
Komatsu, N., Gao, W., Chen, P., Guo, C., Babakhani, A., Kono, J., 2017. Adv. Funct. Mater. 27 (11), 1606022.
Lawal, A.T., 2018. Biosens. Bioelectron. 106, 149–178.
Lee, S.-H., Choe, J.-H., Kim, C., Bae, S., Kim, J.-S., Park, Q.H., Seo, M., 2020. Sensor. Actuator. B Chem. 310, 127841.
Li, B.H., Li, X.W., Zhao, R.Z., Wang, G.C., Han, W.N., Zhao, B.Q., Huang, L.L., Zhang, Y., Lu, Y.F., Jiang, L., 2020. Adv. Opt. Mater. 8 (12), 2000136.
Lin, Y.J., Jarrahi, M., 2020. Rep. Prog. Phys. 83 (6), 066101.
Liu, H., Liu, Y., Zhu, D., 2011. J. Mater. Chem. 21 (10), 3335–3345.
Liu, S.T., Liu, X.P., Chen, J.S., Mao, C.J., Jin, B.K., 2020. Biosens. Bioelectron. 165, 112416.
Mattioli, I.A., Hassan, A., Sanches, N.M., Vieira, N.C.S., Crespilho, F.N., 2021. Biosens. Bioelectron. 175, 112851-112851.
Narasimhan, V., Siddique, R.H., Hoffmann, M., Kumar, S., Choo, H., 2019. Nanoscale 11 (29), 13750–13757.
Niessen, K.A., Xu, M., George, D.K., Chen, M.C., Ferre-D'Amare, A.R., Snell, E.H., Cody, V., Pace, J., Schmidt, M., Markelz, A.G., 2019. Nat. Commun. 10, 1026.
Peng, F., Wang, Z., Yuan, G., Guan, L., Peng, Z., 2018. IEEE Photonics J. 10 (2), 6600808.
Rodrigo, D., Limaj, O., Janner, D., Etezadi, D., Javier Garcia de Abajo, F., Pruneri, V., Altug, H., 2015. Science 349 (6244), 165–168.
Seo, M., Park, H.R., 2019. Adv. Opt. Mater. 8 (3), 1900662.
Shendure, J., Ji, H., 2008. Nat. Biotechnol. 26 (10), 1135–1145.
Singh, R., Al-Naib, I.A.I., Koch, M., Zhang, W., 2011. Opt. Express 19 (7), 6312–6319.
Sousa, T.A.S.L., Santos, F.A., Silva, T.G., Araujo, E.N.D., Plentz, F., 2020. Appl. Surf. Sci. 530, 147003.
Wang, C., Huang, Y., Zhou, R., Xie, L., Ying, Y., 2020a. Opt. Express 28 (8), 12001–12010.
Wang, C., Zhou, R., Huang, Y., Xie, L., Ying, Y., 2019. Food Control 97, 100–104.
Wang, X., Liu, B., Xiao, M., Zou, Y., Lai, W., Pei, H., Alam, M.F., Zhang, W., Wan, Y., Li, L., 2020b. Biosens. Bioelectron. 156, 112130.
Wang, Y., Balgley, J., Gerber, E., Gray, M., Kumar, N., Lu, X., Yan, J.-Q., Fereidouni, A., Basnet, R., Yun, S.J., Suri, D., Kitadai, H., Taniguchi, T., Watanabe, K., Ling, X., Moodera, J., Lee, Y.H., Churchill, H.O.H., Hu, J., Yang, L., Kim, E.-A., Mandrus, D.G., Henriksen, E.A., Burch, K.S., 2020c. Nano Lett. 20 (12), 8446–8452.
Wei, P., Liu, N., Lee, H.R., Adijanto, E., Ci, L., Naab, B.D., Zhong, J.Q., Park, J., Chen, W., Cui, Y., Bao, Z., 2013. Nano Lett. 13 (5), 1890–1897.
Xu, W., Xie, L., Zhu, J., Tang, L., Singh, R., Wang, C., Ma, Y., Chen, H.-T., Ying, Y., 2019. Carbon 141, 247–252.
Yang, X., Zhao, X., Yang, K., Liu, Y., Liu, Y., Fu, W., Luo, Y., 2016. Trends Biotechnol. 34 (10), 810–824.
Yang, Y., Xu, D., Zhang, W., 2018. Opt. Express 26 (24), 31589–31598.
Zeng, S., Sreekanth, K.V., Shang, J., Yu, T., Chen, C.K., Yin, F., Baillargeat, D., Coquet, P., Ho, H.P., Kabashin, A.V., Yong, K.T., 2015. Adv. Mater. 27 (40), 6163–6169.
Zentgraf, T., Meyrath, T.P., Seidel, A., Kaiser, S., Giessen, H., Rockstuhl, C., Lederer, F., 2007. Phys. Rev. B 76 (3), 033407.
Zhang, R., Chen, Q., Liu, K., Chen, Z., Li, K., Zhang, X., Xu, J., Pickwell-MacPherson, E., 2019. IEEE T. THz Sci. Techn. 9 (2), 209–214.
Zhao, Y., Zhang, Y., Shi, Q., Liang, S., Huang, W., Kou, W., Yang, Z., 2018. ACS Photonics 5 (8), 3040–3050.
Zhou, J., Wang, X., Wang, Y., Huang, G., Yang, X., Zhang, Y., Xiong, Y., Liu, L., Zhao, X., Fu, W., 2021. Talanta 228, 122213.
Zhou, R., Wang, C., Huang, Y., Xu, W., Xie, L., Ying, Y., 2020. Opt. Laser. Eng. 133, 106147.
Zhou, R., Wang, C., Xu, W., Xie, L., 2019. Nanoscale 11 (8), 3445–3457.